BLIND POLYCHROMATIC X-RAY CT RECONSTRUCTION FROM POISSON MEASUREMENTS

Renliang Gu and Aleksandar Dogandžić

ECpE Department, Iowa State University
3119 Coover Hall, Ames, IA 50011
email: {renliang,ald}@iastate.edu

ABSTRACT

We develop a sparse image reconstruction method for Poisson-distributed polychromatic X-ray computed tomography (CT) measurements under the blind scenario where the material of the inspected object and the incident energy spectrum are unknown. We employ our mass-attenuation spectrum parameterization of the noiseless measurements for single-material objects and express the mass-attenuation spectrum as a linear combination of B-spline basis functions of order one. A block coordinate-descent algorithm is developed for constrained minimization of a penalized Poisson negative log-likelihood (NLL) cost function, where constraints and penalty terms ensure nonnegativity of the spline coefficients and nonnegativity and sparsity of the density-map image; the image sparsity is imposed using a convex total-variation (TV) norm penalty term. This algorithm alternates between a Nesterov's proximal-gradient (NPG) step for estimating the density-map image and a limited-memory Broyden-Fletcher-Goldfarb-Shanno with box constraints (L-BFGS-B) step for estimating the incident-spectrum parameters. We establish conditions for biconvexity of the penalized NLL objective function, which, if satisfied, ensures monotonicity of the NPG-BFGS iteration. We also show that the penalized NLL objective satisfies the Kurdyka-Łojasiewicz property, which is important for establishing local convergence of block-coordinate descent schemes in biconvex optimization problems. Simulation examples demonstrate the performance of the proposed scheme.

Index Terms— Beam hardening, computed tomography, sparse signal reconstruction, polychromatic X-ray CT.

1. INTRODUCTION

Most polychromatic X-ray computed tomography (CT) reconstruction methods assume known X-ray spectrum and materials (i.e., known mass-attenuation function), with goal to maximize the underlying likelihood function or its regularized version [1, 2]. However, the X-ray spectrum measurements based on the semiconductor detectors are usually distorted by charge trapping, escape events, and other effects [3] and the corresponding correction requires highly collimated beam and special procedures [4, 5]. Knowing the mass-attenuation function can be challenging as well when the inspected material is unknown, or the inspected object is made of compound or mixture with unknown percentage of each constituent. A "blind" scenario for lognormal measurement model with *unknown* incident spectrum and materials is considered in [6]; the methods in [6] use the standard photon-energy parameterization, employ an excessive number of parameters, and suffer from numerical instability [7]. Indeed, iteratively updating excessive numbers of non-identifiable parameters *does not* lead to robust reconstruction schemes.

In this paper, we adopt our parsimonious mass-attenuation spectrum parameterization [8–10] and develop a blind sparse density-map reconstruction scheme from measurements corrupted by Poisson noise. The Poisson noise model is appropriate for measurements from photon-counting detectors and a good approximation for the more precise compound-Poisson distribution for measurements from energy-integrating detectors [11, 12].

Although we focus on Poisson noise and gradient-map image sparsity in this paper, our framework is general and easy to adapt to, for example, lognormal noise and image sparsity in 2D discrete wavelet transform (DWT) domain, see [9, 13].

We introduce the notation: "$\succeq$" is the elementwise version of "$\geq$", $\lceil x \rceil$ is the smallest integer larger than or equal to $x \in \mathbb{R}$, $\mathbb{I}_{[0,+\infty)}(\boldsymbol{\alpha}) = \begin{cases} 0, & \boldsymbol{\alpha} \succeq \mathbf{0} \\ +\infty, & \text{otherwise} \end{cases}$ is the nonnegativity indicator function for a real-valued vector $\boldsymbol{\alpha}$, $\mathrm{dom}(f) = \{\boldsymbol{x} \in \mathbb{R}^n \mid f(\boldsymbol{x}) < +\infty\}$ is the domain of function $f(\cdot)$, and $\boldsymbol{a}^{\mathrm{L}}(s)$ is the *Laplace transform* of a vector function $\boldsymbol{a}(\kappa)$: $\boldsymbol{a}^{\mathrm{L}}(s) = \int \boldsymbol{a}(\kappa) \mathrm{e}^{-s\kappa} \, \mathrm{d}\kappa$. Define also the set of nonnegative real numbers as $\mathbb{R}_+ = [0, +\infty)$, the elementwise logarithm $\ln_\circ \boldsymbol{s} = [\ln s_1, \ldots, \ln s_N]^T$, and Laplace transform $\boldsymbol{a}^{\mathrm{L}}_\circ(\boldsymbol{s}) = \left(\boldsymbol{a}^{\mathrm{L}}(s_n)\right)_{n=1}^N$ obtained by stacking $\boldsymbol{a}^{\mathrm{L}}(s_n)$ columnwise, where $\boldsymbol{s} = [s_1, s_2, \ldots, s_N]^T$.

2. NOISELESS MEASUREMENT MODEL

Denote by N the total number of measurements from all projections collected at the detector array. For the nth measurement, define its discretized line integral as $\boldsymbol{\phi}_n^T \boldsymbol{\alpha}$; stacking all N such integrals into a vector yields $\Phi\boldsymbol{\alpha}$, where $\Phi = [\boldsymbol{\phi}_1 \, \boldsymbol{\phi}_2 \cdots \boldsymbol{\phi}_N]^T \in \mathbb{R}^{N \times p}$ is the known *projection matrix*, also called Radon transform matrix in a parallel-beam X-ray tomographic imaging system. We apply our parsimonious parameterization for single-material inspected objects where, thanks to the separability of the attenuation, we combine the variations of the mass attenuation and X-ray spectrum to construct *mass-attenuation spectrum* $\iota(\kappa)$ [9, 10]. We expand $\iota(\kappa)$ as

$$\iota(\kappa) = \boldsymbol{b}(\kappa)\boldsymbol{\mathcal{I}} \tag{1a}$$

where $\boldsymbol{b}(\kappa)$ are known $1 \times J$ vectors of B-splines of order one (referred to as B1-splines) with knots $\kappa_j = \kappa_0 q^j$ selected from a growing geometric series with common ratio $q > 1$ (see [9, eq. (10c)] for an explicit expression for our B1 splines), J is the number of basis functions, κ denotes the mass attenuation, and

This work was supported by the National Science Foundation under Grant CCF-1421480.

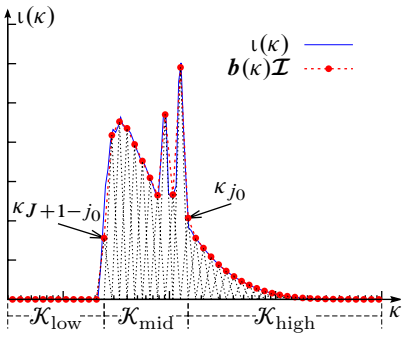

Fig. 1: B1-spline expansion of mass-attenuation spectrum $\iota(\kappa)$.

$\boldsymbol{\mathcal{I}} = [\mathcal{I}_1, \mathcal{I}_2, \ldots, \mathcal{I}_J]^T \succeq \mathbf{0}$ is an *unknown* $J \times 1$ vector of corresponding basis-function coefficients. The common ratio q determines the resolution of the B-spline approximation and expanding $\iota(\kappa)$ in B1-spline basis means that $\iota(\kappa)$ is modeled as piecewise-linear with endpoints of linear segments at $(\mathcal{I}_j)_{j=1}^J$, see Fig. 1.

We obtain the following expression for the $N \times 1$ vector of noiseless X-ray CT energy measurements [9, eq. (11b)]:

$$\boldsymbol{\mathcal{I}}^{\text{out}}(\boldsymbol{\alpha}, \boldsymbol{\mathcal{I}}) = \boldsymbol{b}_\circ^{\text{L}}(\Phi\boldsymbol{\alpha})\boldsymbol{\mathcal{I}} \tag{1b}$$

where $\boldsymbol{\alpha} = (\alpha_i)_{i=1}^p \succeq \mathbf{0}$ is an *unknown* $p \times 1$ vector representing the 2D image that we wish to reconstruct and $\boldsymbol{b}_\circ^{\text{L}}(s)$ is an *output basis-function matrix* obtained by stacking the $1 \times J$ vectors $\boldsymbol{b}^{\text{L}}(s_n)$ columnwise.

3. MEASUREMENT MODEL AND PENALIZED NLL OBJECTIVE FUNCTION

For an $N \times 1$ vector $\boldsymbol{\mathcal{E}} = (\mathcal{E}_n)_{n=1}^N$ of independent Poisson measurements, the negative log-likelihood (NLL) in the form of generalized Kullback-Leibler divergence [14] is [see also (1b)]

$$\mathcal{L}(\boldsymbol{\alpha}, \boldsymbol{\mathcal{I}}) = \mathbf{1}^T \left[\boldsymbol{\mathcal{I}}^{\text{out}}(\boldsymbol{\alpha}, \boldsymbol{\mathcal{I}}) - \boldsymbol{\mathcal{E}}\right] - \sum_{n, \mathcal{E}_n \neq 0} \mathcal{E}_n \ln \frac{\mathcal{I}_n^{\text{out}}(\boldsymbol{\alpha}, \boldsymbol{\mathcal{I}})}{\mathcal{E}_n}. \tag{2}$$

We now express (2) as a function of $\boldsymbol{\alpha}$ with $\boldsymbol{\mathcal{I}}$ fixed and vice versa, which will be used to describe our estimation algorithm:

$$\mathcal{L}_\iota(\boldsymbol{\alpha}) = \mathbf{1}^T \left[\iota_\circ^{\text{L}}(\Phi\boldsymbol{\alpha}) - \boldsymbol{\mathcal{E}}\right] - \sum_{n, \mathcal{E}_n \neq 0} \mathcal{E}_n \ln \frac{\iota^{\text{L}}(\boldsymbol{\phi}_n^T \boldsymbol{\alpha})}{\mathcal{E}_n} \tag{3a}$$

$$\mathcal{L}_A(\boldsymbol{\mathcal{I}}) = \mathbf{1}^T (A\boldsymbol{\mathcal{I}} - \boldsymbol{\mathcal{E}}) - \sum_{n, \mathcal{E}_n \neq 0} \mathcal{E}_n \ln \frac{[A\boldsymbol{\mathcal{I}}]_n}{\mathcal{E}_n} \tag{3b}$$

where $A \triangleq \boldsymbol{b}_\circ^{\text{L}}(\Phi\boldsymbol{\alpha})$ is defined in the case where $\boldsymbol{\alpha}$ is fixed. Here, (3a) corresponds to the Poisson generalized linear model (GLM) [15] with design matrix Φ and link function equal to the inverse of $\iota^{\text{L}}(\cdot)$ and (3b) corresponds to the Poisson GLM with design matrix A and identity link.

Theorem 1. *The NLL* (2) *is biconvex with respect to* $\boldsymbol{\alpha}$ *and* $\boldsymbol{\mathcal{I}}$ *in the following set:*

$$\left\{(\boldsymbol{\alpha}, \boldsymbol{\mathcal{I}}) \,\middle|\, \boldsymbol{\mathcal{I}}^{\text{out}}(\boldsymbol{\alpha}, \boldsymbol{\mathcal{I}}) \succeq \frac{(q^{j_0} - 1)^2}{q^{2j_0} + 1} \boldsymbol{\mathcal{E}},\ \boldsymbol{\mathcal{I}} \in \mathcal{A},\ \boldsymbol{\alpha} \in \mathbb{R}_+^p \right\} \tag{4a}$$

which bounds $\mathcal{I}_n^{\text{out}}(\boldsymbol{\alpha}, \boldsymbol{\mathcal{I}})/\mathcal{E}_n$ *from below for all* n. *Here, we constrain the region of allowed* $\boldsymbol{\mathcal{I}}$ *to*

$$\mathcal{A} = \Big\{\boldsymbol{\mathcal{I}} \in \mathbb{R}_+^J \,\Big|\, \mathcal{I}_1 \leq \mathcal{I}_2 \leq \cdots \leq \mathcal{I}_{J+1-j_0},\ \mathcal{I}_{j_0} \geq \cdots \geq \mathcal{I}_J,\ \text{and } \mathcal{I}_j \geq \mathcal{I}_{J+1-j_0},\ \forall\, j \in [J+1-j_0, j_0]\Big\} \tag{4b}$$

which imposes monotonicity of the mass-attenuation spectrum $\iota(\kappa)$ *in low- and high-*κ *regions determined by the constant* $j_0 \geq \lceil (J+1)/2 \rceil$ *and also that the mid-*κ *region has higher spectrum than the low-*κ *region, see Fig. 1.*

Proof: We outline main steps of the proof, see [9] for details. We first prove that the region specified by (4a) is biconvex with respect to $\boldsymbol{\alpha}$ and $\boldsymbol{\mathcal{I}}$. We then show that the NLL $\mathcal{L}_A(\boldsymbol{\mathcal{I}})$ is convex over $\boldsymbol{\mathcal{I}}$ simply by taking the second derivative of $\mathcal{L}_A(\boldsymbol{\mathcal{I}})$ and verifying that the resulting Hessian matrix is always positive semidefinite. Finally, we show that the Hessian matrix of $\mathcal{L}_\iota(\boldsymbol{\alpha})$ has the form $\Psi\Lambda\Psi^T$ where Λ is a diagonal matrix whose elements are nonnegative in the region (4a). □

In practice, the X-ray spectrum $\iota(\varepsilon)$ starts at the lowest effective energy that can penetrate the object, vanishes at the tube voltage (the highest photon energy), and has a region in the center higher than the two ends; see Fig. 2b. When the support of $\iota(\varepsilon)$ is free of K-edges, the mass-attenuation coefficient $\kappa(\varepsilon)$ is a monotonic function of ε; thus $\iota(\kappa)$ as a function of κ has similar shape as $\iota(\varepsilon)$ as a function of ε, which justifies assumption (4b). If a K-edge is present within the support of $\iota(\varepsilon)$, it is difficult to infer the shape of $\iota(\kappa)$. In most cases, (4b) holds.

Our goal is to compute penalized maximum-likelihood estimates of the density-map and mass-attenuation spectrum parameters $(\boldsymbol{\alpha}, \boldsymbol{\mathcal{I}})$ by solving the following minimization problem:

$$\min_{\boldsymbol{\alpha}, \boldsymbol{\mathcal{I}}} f(\boldsymbol{\alpha}, \boldsymbol{\mathcal{I}}) \tag{5}$$

where

$$f(\boldsymbol{\alpha}, \boldsymbol{\mathcal{I}}) = \mathcal{L}(\boldsymbol{\alpha}, \boldsymbol{\mathcal{I}}) + u r(\boldsymbol{\alpha}) + \mathbb{I}_{[0,+\infty)}(\boldsymbol{\mathcal{I}}) \tag{6a}$$

$$r(\boldsymbol{\alpha}) = \sum_{i=1}^p \sqrt{\sum_{j \in \mathcal{N}_i} (\alpha_i - \alpha_j)^2} + \mathbb{I}_{[0,+\infty)}(\boldsymbol{\alpha}) \tag{6b}$$

are the penalized NLL objective function and the density-map regularization term that enforces nonnegativity and sparsity of the signal $\boldsymbol{\alpha}$ in the total-variation (TV) domain. Here, $u > 0$ is a scalar tuning constant and $\mathcal{N}_i$ is index set of neighbors of α_i, where the elements of $\boldsymbol{\alpha}$ are arranged to form a 2D image [16].

3.1. Properties of the objective function $f(\boldsymbol{\alpha}, \boldsymbol{\mathcal{I}})$

Since $r(\boldsymbol{\alpha})$ in (6b) and $\mathbb{I}_{[0,+\infty)}(\boldsymbol{\mathcal{I}})$ in (6a) are convex functions of $\boldsymbol{\alpha}$ and $\boldsymbol{\mathcal{I}}$ for all $\boldsymbol{\alpha} \succeq \mathbf{0}$ and $\boldsymbol{\mathcal{I}} \succeq \mathbf{0}$, the following holds:

Corollary 1. *The objective* $f(\boldsymbol{\alpha}, \boldsymbol{\mathcal{I}})$ *in* (6a) *is biconvex with respect to* $\boldsymbol{\alpha}$ *and* $\boldsymbol{\mathcal{I}}$ *under the conditions specified by Theorem 1.*

We now establish that the objective function (6a) satisfies the Kurdyka-Łojasiewicz (KL) property provided that the incident X-ray source is nonzero.

Theorem 2 (KL Property)**.** *The objective function* $f(\boldsymbol{\alpha}, \boldsymbol{\mathcal{I}})$ *satisfies the KL property in any compact subset* $\mathbb{C} \subseteq \text{dom}(f)$.

Proof: We show that the NLL in (2) is real-analytic for all $\boldsymbol{\alpha}$ in a compact subset $\mathbb{C}$ in the domain of $f(\boldsymbol{\alpha}, \boldsymbol{\mathcal{I}})$; both $r(\boldsymbol{\alpha})$ in (6b) and $\mathbb{I}_{[0,+\infty)}(\boldsymbol{\mathcal{I}})$ are semialgebraic functions. The sum of

real-analytic and semi-algebraic functions is sub-analytic, which implies the KL property of $f(\boldsymbol{\alpha}, \mathcal{I})$ [17, Sec. 2.2]. See [9] for details. □

4. MINIMIZATION ALGORITHM

Iteration i for minimizing (6a) updates $\boldsymbol{\alpha}$ and $\mathcal{I}$ alternatively:

1) (NPG) Set the mass-attenuation spectrum $\iota(\kappa) = \boldsymbol{b}(\kappa)\mathcal{I}^{(i-1)}$, treat it as known, and descend the regularized NLL function $f(\boldsymbol{\alpha}, \mathcal{I}^{(i-1)}) = \mathcal{L}_\iota(\boldsymbol{\alpha}) + ur(\boldsymbol{\alpha})$ [see (3a)] by applying a *Nesterov's proximal-gradient (NPG) step* [18, 19] for $\boldsymbol{\alpha}$:

$$\theta^{(i)} = \frac{1}{2}\left[1 + \sqrt{1 + 4\left(\theta^{(i-1)}\right)^2}\right] \tag{7a}$$

$$\bar{\boldsymbol{\alpha}}^{(i)} = \boldsymbol{\alpha}^{(i-1)} + \frac{\theta^{(i-1)} - 1}{\theta^{(i)}}\left(\boldsymbol{\alpha}^{(i-1)} - \boldsymbol{\alpha}^{(i-2)}\right) \tag{7b}$$

$$\boldsymbol{\alpha}^{(i)} = \arg\min_{\boldsymbol{\alpha}} \frac{1}{2\beta^{(i)}}\left\|\boldsymbol{\alpha} - \bar{\boldsymbol{\alpha}}^{(i)} + \beta^{(i)}\nabla\mathcal{L}_\iota\left(\bar{\boldsymbol{\alpha}}^{(i)}\right)\right\|_2^2 + ur(\boldsymbol{\alpha}) \tag{7c}$$

where the minimization (7c) is computed using an inner iteration that employs the TV-based denoising method in [16, Sec. IV] and $\beta^{(i)} > 0$ is an adaptive step size chosen to satisfy the majorization condition:

$$\mathcal{L}_\iota\left(\boldsymbol{\alpha}^{(i)}\right) \le \mathcal{L}_\iota\left(\bar{\boldsymbol{\alpha}}^{(i)}\right) + \left(\boldsymbol{\alpha}^{(i)} - \bar{\boldsymbol{\alpha}}^{(i)}\right)^T\nabla\mathcal{L}_\iota\left(\bar{\boldsymbol{\alpha}}^{(i)}\right) + \frac{1}{2\beta^{(i)}}\left\|\boldsymbol{\alpha}^{(i)} - \bar{\boldsymbol{\alpha}}^{(i)}\right\|_2^2 \tag{7d}$$

using a patient adaptation scheme that aims at finding the largest $\beta^{(i)}$ that satisfies (7d), see [20] for details. We select the initial step size $\beta^{(0)}$ using the Barzilai-Borwein (BB) method [21] and apply the *function restart* [22] to restore the monotonicity and improve convergence of NPG steps.

2) (BFGS) Set the design matrix $A = \boldsymbol{b}_\circ^{\mathrm{L}}(\Phi\boldsymbol{\alpha}^{(i)})$, treat it as known, and minimize the regularized NLL function $f\left(\boldsymbol{\alpha}^{(i)}, \mathcal{I}\right)$ with respect to $\mathcal{I}$, i.e., solve [see (3b)]

$$\mathcal{I}^{(i)} = \arg\min_{\mathcal{I}\succeq\mathbf{0}} \mathcal{L}_A(\mathcal{I}) \tag{8}$$

using the inner limited-memory Broyden-Fletcher-Goldfarb-Shanno with box constraints (L-BFGS-B) iteration [23], initialized by $\mathcal{I}^{(i-1)}$.

Iterate between Steps 1 and 2 until the relative distance of consecutive iterates of the density map $\boldsymbol{\alpha}$ does not change significantly:

$$\left\|\boldsymbol{\alpha}^{(i)} - \boldsymbol{\alpha}^{(i-1)}\right\|_2 < \epsilon\left\|\boldsymbol{\alpha}^{(i)}\right\|_2 \tag{9}$$

where $\epsilon > 0$ is the convergence threshold. The convergence criteria for the inner TV-denoising and L-BFGS-B iterations are chosen to trade off the accuracy and speed of the inner iterations and provide sufficiently accurate solutions to (7c) and (8).

We refer to the iteration between Steps 1 and 2 as the *NPG-BFGS algorithm*: it is the first physical-model–based image reconstruction method for simultaneous *blind* (assuming unknown incident X-ray spectrum and unknown materials) sparse image reconstruction and mass-attenuation spectrum estimation from polychromatic measurements. If the mass-attenuation spectrum $\iota(\kappa)$ is *known* and we iterate Step 1 only to estimate the density-map $\boldsymbol{\alpha}$, we refer to this iteration as the *NPG algorithm (known $\iota(\kappa)$)*.

If we *do not* apply the Nesterov's acceleration (7a)–(7b) and use only the proximal-gradient (PG) step (7c) to update the density-map iterates $\boldsymbol{\alpha}$, i.e., assign $\bar{\boldsymbol{\alpha}}^{(i)} = \boldsymbol{\alpha}^{(i-1)}$ instead of (7b), we refer to the corresponding iteration as the *PG-BFGS algorithm*.

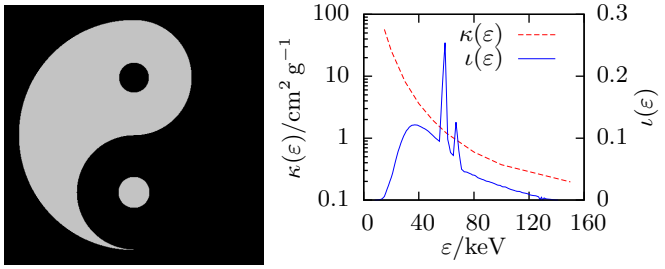

(a) (b)

Fig. 2: (a) Density-map image and (b) mass attenuation and incident X-ray spectrum as functions of the photon energy ε.

Remark 1 (Monotonicity)**.** *Under the condition* (4a) *of Theorem 1, the NPG-BFGS iteration with function restart is monotonically non-increasing:*

$$f\left(\boldsymbol{\alpha}^{(i)}, \mathcal{I}^{(i)}\right) \le f\left(\boldsymbol{\alpha}^{(i-1)}, \mathcal{I}^{(i-1)}\right) \tag{10}$$

for all i.

Proof: Step 1 is monotonic thanks to either the function restart or the convexity of $f(\boldsymbol{\alpha}, \mathcal{I})$ over $\boldsymbol{\alpha}$ combined with the condition (7d), Step 2 is monotonic by (8). Hence, each step of the NPG-BFGS iteration is monotonic. □

Based on Theorem 2, we establish critical-point convergence of PG-BFGS using arguments along the lines of [17], see [9, Th. 3].

5. NUMERICAL EXAMPLES

Consider reconstruction of the 512×512 image in Fig. 2a of an iron object with density map $\boldsymbol{\alpha}_{\text{true}}$. We generated a fan-beam polychromatic sinogram, with distance from X-ray source to the rotation center equal to 2000 times the pixel size, using the interpolated mass attenuation $\kappa(\varepsilon)$ of iron [24] and incident spectrum $\iota(\varepsilon)$ from tungsten anode X-ray tubes at 140 keV with 5 % relative voltage ripple [25], see Fig. 2b. Our simulated approximation of the noiseless measurements uses 130 equi-spaced discretization points over the range 20 keV to 140 keV. We simulated independent Poisson measurements $(\mathcal{E}_n)_{n=1}^N$ with means $(\mathrm{E}\,\mathcal{E}_n)_{n=1}^N = \mathcal{I}^{\text{out}}(\boldsymbol{\alpha}, \mathcal{I})$. We mimic real X-ray CT system calibration by scaling the projection matrix Φ and the spectrum $\iota(\varepsilon)$ so that the maximum and minimum of the noiseless measurements $(\mathrm{E}\,\mathcal{E}_n)_{n=1}^N$ are 2^{16} and 20, respectively. Here, the scales of Φ and $\iota(\varepsilon)$ correspond to the real size that each image pixel represents and the current of the electrons hitting the tungsten anode as well as the overall scanning time.

We use the relative square error (RSE), $1 - \left(\frac{\widehat{\boldsymbol{\alpha}}^T\boldsymbol{\alpha}_{\text{true}}}{\|\widehat{\boldsymbol{\alpha}}\|_2\|\boldsymbol{\alpha}_{\text{true}}\|_2}\right)^2$ as the reconstruction performance metric; RSE is invariant to scaling $\widehat{\boldsymbol{\alpha}}$ by a nonzero constant, which is needed because the magnitude level of $\boldsymbol{\alpha}$ is not identifiable by our blind approach [8–10]. We compare

i) our
   - NPG-BFGS method with $J = 30$ spline basis functions spanning three orders of magnitude,

(a) FBP (b) linearized FBP (c) linearized BPDN (d) NPG (known $\iota(\kappa)$) (e) NPG-BFGS

Fig. 3: Reconstructions from 60 projections.

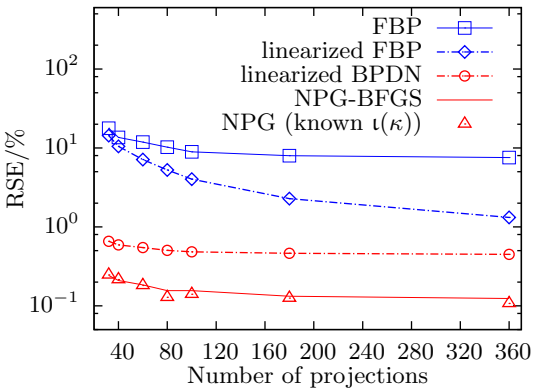

Fig. 4: Average RSEs as functions of the number of projections.

- NPG for known mass attenuation spectrum $\iota(\kappa)$ (Matlab implementation at github.com/isucsp/imgRecSrc);

ii) linearized basis pursuit denoising (linearized BPDN), which applies the NPG approach to solve the basis pursuit denoising (BPDN) problem [16]: $\min_{\boldsymbol{\alpha}} 0.5\|\boldsymbol{y}-\Phi\boldsymbol{\alpha}\|_2^2+u'r(\boldsymbol{\alpha})$, where $\boldsymbol{y}=\left(\iota^{\mathrm{L}}\right)_{\circ}^{-1}(\boldsymbol{\mathcal{E}})$ are the linearized measurements and $u'>0$ is the regularization constant,

iii) the traditional filtered backprojection (FBP) method without [26, Ch. 3] and with linearization [27], i.e., based on the 'data' $\boldsymbol{y}=-\ln_{\circ}\boldsymbol{\mathcal{E}}$ and $\boldsymbol{y}=\left(\iota^{\mathrm{L}}\right)_{\circ}^{-1}(\boldsymbol{\mathcal{E}})$, respectively.

For all methods that use sparsity and nonnegativity regularization (NPG-BFGS, NPG, and linearized BPDN), the regularization constants u and u' have been tuned manually for best average RSE performance. All iterative algorithms employ the convergence criterion (9) with threshold $\epsilon=10^{-6}$ and the maximum number of iterations set to 4000. We initialize iterative reconstruction schemes with or without linearization using the corresponding FBP reconstructions.

The *non-blind* linearized FBP, NPG (known $\iota(\kappa)$), and linearized BPDN methods rely on knowledge of $\iota(\kappa)$ [which requires knowledge of the incident spectrum of the X-ray machine and mass attenuation (material)], which we computed using (1a) with $\mathcal{I}$ equal to the exact sampled $\iota(\kappa)$ and $J=100$ spline basis functions spanning three orders of magnitude. Neither FBP nor NPG-BFGS assume knowledge of the mass-attenuation spectrum $\iota(\kappa)$: FBP *ignores* the polychromatic-source effects whereas NPG-BFGS corrects *blindly* for these effects *without* knowledge of $\iota(\kappa)$.

Fig. 3 shows the reconstructions from 60 equi-spaced fan-beam projections with spacing 6°, using one realization of noisy Poisson measurements. The FBP reconstruction in Fig. 3a exhibits both aliasing and beam-hardening (cupping and streaking) artifacts. Linearized FBP, which assumes perfect knowledge of the mass-attenuation spectrum, performs better than FBP, removes the beam-hardening but retains the aliasing artifacts, and yields noisy reconstruction due to the zero-forcing nature of linearization, see Fig. 3b. Thanks to enforcing the nonnegativity and sparsity constraints, linearized BPDN removes the aliasing artifacts and the negative signal components, and achieves a smooth reconstruction with a 0.55 % RSE. NPG-BFGS and NPG account for both the polychromatic X-ray source and Poisson noise and handle the noisy measurements in a statistically optimal manner, thereby achieving the best reconstructions, see Figs. 3d and 3e.

Fig. 4 shows the average RSEs (over 5 Poisson noise realizations) of different methods as functions of the number of fan-beam projections in the range from 0° to 359°. Average RSEs of the methods that do not assume knowledge of the mass-attenuation spectrum $\iota(\kappa)$ are shown using solid lines whereas dashed lines represent methods that assume known $\iota(\kappa)$. Red and blue colors present methods that *do* and *do not* employ signal-sparsity regularization, respectively. FBP ignores the polychromatic nature of the measurements and consequently performs poorly and does not improve as the number of projections increases. Linearized FBP, which assumes perfect knowledge of the mass attenuation spectrum, performs better than FBP, as shown in Fig. 4. Linearized BPDN attains up to 20 times better RSE than linearized FBP thanks to the nonnegativity and sparsity that it imposes on the signal; however, the zero-forcing nature of the linearization process leads to noise enhancement, which ultimately limits the reconstruction performance of linearized BPDN. As expected, NPG is slightly better than NPG-BFGS because it assumes knowledge of $\iota(\kappa)$. NPG and NPG-BFGS attain RSEs that are 24 % to 37 % that of linearized BPDN, which can be attributed to optimal statistical processing of the proposed methods, in contrast with suboptimal linearization. It is remarkable that the blind NPG-BFGS method effectively matches the performance of NPG (known $\iota(\kappa)$).

See [8, 9] for reconstructions using real X-ray CT data.

6. CONCLUSION

We developed a sparse polychromatic X-ray CT reconstruction method from Poisson measurements that requires no additional information than the conventional FBP method, and yet is capable of correcting beam-hardening *and* aliasing artifacts. We established conditions for biconvexity of the underlying penalized negative log-likelihood function with respect to the unknown density-map and mass-attenuation spectrum parameters, and analyzed properties of the proposed reconstruction scheme.

References

[1] I. A. Elbakri and J. A. Fessler, "Statistical image reconstruction for polyenergetic X-ray computed tomography," *IEEE Trans. Med. Imag.*, vol. 21, no. 2, pp. 89–99, 2002.

[2] J. D. Evans, B. R. Whiting, D. G. Politte, J. A. O'Sullivan, P. F. Klahr, and J. F. Williamson, "Experimental implementation of a polyenergetic statistical reconstruction algorithm for a commercial fan-beam CT scanner," *Phys. Medica*, vol. 29, no. 5, pp. 500–512, 2013.

[3] R. Redus, J. Pantazis, T. Pantazis, A. Huber, and B. Cross, "Characterization of CdTe detectors for quantitative X-ray spectroscopy," *IEEE Trans. Nucl. Sci.*, vol. 56, no. 4, pp. 2524–2532, 2009.

[4] D. Zhang, X. Li, and B. Liu, "X-ray spectral measurements for tungsten-anode from 20 to 49 kVp on a digital breast tomosynthesis system," *Med. Phys.*, vol. 39, no. 6, pp. 3493–3500, 2012.

[5] Y. Lin, J. C. Ramirez-Giraldo, D. J. Gauthier, K. Stierstorfer, and E. Samei, "An angle-dependent estimation of CT x-ray spectrum from rotational transmission measurements," *Med. Phys.*, vol. 41, no. 6, p. 062 104, 2014.

[6] G. Van Gompel, K. Van Slambrouck, M. Defrise, K. Batenburg, J. de Mey, J. Sijbers, and J. Nuyts, "Iterative correction of beam hardening artifacts in CT," *Med. Phys.*, vol. 38, S36–S49, 2011.

[7] R. Gu and A. Dogandžić, "Sparse X-ray CT image reconstruction and blind beam hardening correction via mass attenuation discretization," in *Proc. IEEE Int. Workshop Comput. Advances Multi-Sensor Adaptive Process.*, Saint Martin, French West Indies, Dec. 2013, pp. 244–247.

[8] ——, "Blind X-ray CT image reconstruction from polychromatic Poisson measurements," *IEEE Trans. Comput. Imag.*, vol. 2, no. 2, pp. 150–165, 2016.

[9] ——, (Sep. 2015). Polychromatic X-ray CT image reconstruction and mass-attenuation spectrum estimation. arXiv: 1509.02193 [stat.ME].

[10] ——, "Beam hardening correction via mass attenuation discretization," in *Proc. IEEE Int. Conf. Acoust., Speech, Signal Process.*, Vancouver, Canada, May 2013, pp. 1085–1089.

[11] J. Xu and B. M. Tsui, "Quantifying the importance of the statistical assumption in statistical X-ray CT image reconstruction," *IEEE Trans. Med. Imag.*, vol. 33, no. 1, pp. 61–73, 2014.

[12] G. M. Lasio, B. R. Whiting, and J. F. Williamson, "Statistical reconstruction for X-ray computed tomography using energy-integrating detectors," *Phys. Med. Biol.*, vol. 52, no. 8, p. 2247, 2007.

[13] R. Gu and A. Dogandžić, "Polychromatic sparse image reconstruction and mass attenuation spectrum estimation via B-spline basis function expansion," in *Rev. Prog. Quant. Nondestr. Eval.*, D. E. Chimenti and L. J. Bond, Eds., ser. AIP Conf. Proc. Vol. 34 1650, Melville, NY, 2015, pp. 1707–1716.

[14] L. Zanni, A. Benfenati, M. Bertero, and V. Ruggiero, "Numerical methods for parameter estimation in Poisson data inversion," *J. Math. Imaging Vis.*, vol. 52, no. 3, pp. 397–413, 2015.

[15] P. McCullagh and J. Nelder, *Generalized Linear Models*, 2nd ed. New York: Chapman & Hall, 1989.

[16] A. Beck and M. Teboulle, "Fast gradient-based algorithms for constrained total variation image denoising and deblurring problems," *IEEE Trans. Image Process.*, vol. 18, no. 11, pp. 2419–2434, 2009.

[17] Y. Xu and W. Yin, "A block coordinate descent method for regularized multiconvex optimization with applications to nonnegative tensor factorization and completion," *SIAM J. Imag. Sci.*, vol. 6, no. 3, pp. 1758–1789, 2013.

[18] Y. Nesterov, "A method of solving a convex programming problem with convergence rate $O(1/k^2)$," in *Sov. Math. Dokl.*, vol. 27, 1983, pp. 372–376.

[19] A. Beck and M. Teboulle, "A fast iterative shrinkage-thresholding algorithm for linear inverse problems," *SIAM J. Imag. Sci.*, vol. 2, no. 1, pp. 183–202, 2009.

[20] R. Gu and A. Dogandžić, "Projected Nesterov's proximal-gradient signal recovery from compressive Poisson measurements," in *Proc. Asilomar Conf. Signals, Syst. Comput.*, Pacific Grove, CA, Nov. 2015, pp. 1490–1495.

[21] J. Barzilai and J. M. Borwein, "Two-point step size gradient methods," *IMA J. Numer. Anal.*, vol. 8, no. 1, pp. 141–148, 1988.

[22] B. O'Donoghue and E. Candès, "Adaptive restart for accelerated gradient schemes," *Found. Comput. Math.*, vol. 15, no. 3, pp. 715–732, 2013.

[23] R. H. Byrd, P. Lu, J. Nocedal, and C. Zhu, "A limited memory algorithm for bound constrained optimization," *SIAM J. Sci. Comput.*, vol. 16, no. 5, pp. 1190–1208, 1995.

[24] J. H. Hubbell and S. M. Seltzer, "Tables of X-ray mass attenuation coefficients and mass energy-absorption coefficients 1 keV to 20 MeV for elements $Z = 1$ to 92 and 48 additional substances of dosimetric interest," National Inst. Standards Technol., Ionizing Radiation Div., Gaithersburg, MD, Tech. Rep. NISTIR 5632, 1995.

[25] J. M. Boone and J. A. Seibert, "An accurate method for computer-generating tungsten anode X-ray spectra from 30 to 140 kV," *Med. Phys.*, vol. 24, no. 11, pp. 1661–1670, 1997.

[26] A. C. Kak and M. Slaney, *Principles of Computerized Tomographic Imaging*. New York: IEEE Press, 1988.

[27] G. T. Herman, "Correction for beam hardening in computed tomography," *Phys. Med. Biol.*, vol. 24, no. 1, pp. 81–106, 1979.